Available online at www.sciencedirect.com
SCIENCE DIRECT
Catalysis Today 102–103 (2005) 2–14
CATALYSIS TODAY
www.elsevier.com/locate/cattod

Carbon nanostructures with macroscopic shaping for catalytic applications

Marc-Jacques Ledoux *, Cuong Pham-Huu

Laboratoire des Matériaux, Surfaces et Procédés pour la Catalyse, UMR 7515 du CNRS, ECPM, ULP ELCASS (European Laboratory for Catalysis and Surface Science) 25, rue Becquerel, 67037 Strasbourg Cedex 2, France

Available online 12 April 2005

Abstract

Carbon nanostructures, nanofibers and nanotubes, with a 1D dimension have witnessed, during the last decade, a large scientific and industrial interest owing to their exceptional physical and chemical properties. Among the different potential applications the use of these carbon nanostructures as catalyst support material seems to be one of the most promising.

In the present work, the synthesis and characterisation of a new type of carbon nanofibers (CNF) composite with macroscopic shaping is reported. The CNF composite obtained can be tailored into different macroscopic shapes allowing it to be directly employed in the existing conventional reactors without the problems linked to the small size of the unsupported carbon nanofibers. This material displays a relatively high surface area $>100\ m^2\ g^{-1}$, essentially constituted by the external surface, and a complete absence of the bottled pores encountered with traditional solid carriers such as alumina, silica or activated charcoal.

The as-synthesized CNF composite was subsequently tested as catalyst support in two reactions, i.e. the catalytic decomposition of hydrazine and the selective oxidation of H_2S into elemental sulfur, where its catalytic performance was largely superior to that obtained on the state-of-the-art traditional catalysts.

Keywords: Synthesis; Carbon nanofibers; Macroscopic shape; Decomposition of hydrazine; Selective oxidation of H_2S

1. Catalysis and carbon

Catalysis plays an important role in the processing of several vital compounds in numerous fields such as fuels, fine chemicals and pollution abatment. Today, much research is still being conducted in order to enhance catalytic activity and selectivity and reduce the cost of catalyst preparation. In parallel with the development of new active phase formulations, intensive research has also been conducted both in academic and industrial groups in order to develop new catalyst supports which can modify the catalytic activity and selectivity of the existing active phase. Recent research has demonstrated significant improvement in both the catalytic activity and product selectivity in numerous reactions, e.g. selective isomerisation of *n*-alkanes, partial oxidation of light alkanes into valuable products or for the Claus tail-gas process, using a medium surface area silicon carbide (β-SiC), crystalllised in a cubic structure, as support material [1,2]. Another promising new catalyst support is carbon in its nanosize structures.

Consecutive to the discovery of carbon nanotubes by Iijima [3], the carbon nanomaterials, nanotubes and nanofibers, have received increasing academic and industrial interest during the last decade owing to their exceptional physical and chemical properties [4–6]. Theoretical calculations and experiments have predicted a large domain of applications for these nanomaterials going from nanoelectronic components to biological applications. Amongst these, catalysis seems to be the most direct and promising field according to the results published during the last years [7–15]. Carbon nanomaterials generally exhibit catalytic performances higher than those encountered with traditional catalysts whatever the reactions considered, i.e. gas phase or liquid phase. It is thought that the tailoring of nanostructured

* Corresponding author. Tel.: +33 3 90 24 26 75; fax: +33 3 90 24 26 74.
E-mail addresses: ledoux@cournot.u-strasbg.fr (M.-J. Ledoux), cuong.lcmc@ecpm.u-strasbg.fr (C. Pham-Huu).

0920-5861/$ – see front matter © 2005 Elsevier B.V. All rights reserved.
doi:10.1016/j.cattod.2005.02.036

catalysts, carbon nanofibers and carbon nanotubes, with a peculiar morphology, i.e. high length-to-diameter ratio (aspect ratio), tubular structure in the case of carbon nanotubes with possible confinement effect [16], high external surface area and absence of any 2D porosity, could lead to new electronic interactions and to a higher accessibility of the reactants to the deposited active phase, and consequently, improve the catalytic properties of the carbon nanostructure-based catalysts when compared to those usually obtained up to now with traditional catalysts [17,18].

2. Carbon nanostructures (nanofibers and nanotubes) materials

Carbon nanofilaments, nanotubes if hollow and nanofibers if filled, have already been detected several decades ago essentially as poison for natural gas steam-reforming catalysts. The main work devoted to the synthesis and catalytic applications of carbon nanofibers originated essentially from Baker's group [8,9,19–24]. The carbon nanofibers-based catalyst exhibits higher performance when compared to those observed on traditional catalysts, i.e. carbon or alumina, in several reactions including olefin hydrogenation. A carbon nanofiber structure consists of a stacking of different graphite sheets oriented at an angle with respect to the fiber axis and no open tubule in the middle, as shown in Fig. 1A. The exposed surface of the carbon nanofiber mainly consists of prismatic planes with high surface reactivity when compared to the basal planes of graphite. It is worth noting that the carbon nanofiber structure from one fiber to another is relatively heterogeneous. The high reactivity of the prismatic planes of the carbon nanofiber surface was evidenced by its lower stability towards oxygen when compared to that observed on graphite material [7].

For the carbon nanotubes, i.e. tubular carbon structure consisting of cylindrical graphene layers with a hollow internal cavity, their interest has only been launched since their discovery in 1991 by Iijima [3] as by-product of arc-discharge materials. Carbon nanotubes then received increasing scientific and industrial interest for their unique physical and chemical properties, which render them attractive in several potential applications in electronics, mechanicals and catalysis fields [4–6,25–29]. The structure of the carbon nanotubes can be directly related to that of the fullerene containing 60 carbon atoms arranged in a sphere. The elongation of the fullerene leads to single walled carbon nanotubes (SWNTs) with diameters of approximately 1 nm. The multi-walled carbon nanotubes (MWNTs) are created by the superposition of several graphene cylinders concentrically rolled-up on each other. An image of a carbon nanotube, i.e. MWNT, is displayed in Fig. 1B. The interlayer spacing in MWNT is slightly larger than the one observed in a single crystal of graphite, i.e. 0.34 nm instead of 0.335 nm, due to the geometrical constraint induced by the concentric structure of the carbon nanotube.

The possibility for using these carbon nanostructured materials in industrial applications seems nowadays to be nearer, owing to the possibility to synthesize them in large quantities without too many by-products such as onion or amorphous carbon through the chemical vapour deposition (CVD) method [5,7,15,30,31]. The CVD method allows the synthesis of carbon nanostructures, i.e. nanotubes or nanofibers, with a relatively high yield at low reaction temperature using supported catalysts based on Ni, Fe or Co. The mass production of these materials would lead to a significant decrease in their price, rendering them more and

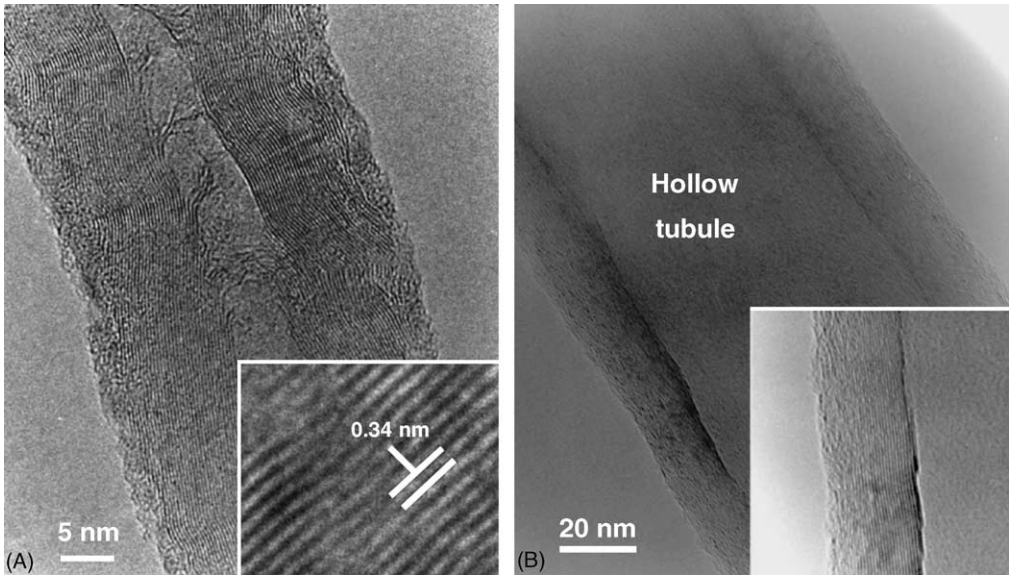

Fig. 1. Representative TEM image of (A) carbon nanofibers with the fishbone stacking of graphene planes along the fiber axis and (B) carbon nanotubes with hollow tubule and graphene planes stacking parallel to the tube axis. These nanostructured carbon materials were synthesized from the chemical vapour deposition at temperature lower than 800 °C which lead to the occurrence of a large number of defects along the growth axis.

more competitive compared to the traditional support carriers such as alumina, silica, activated charcoal, etc.

3. Catalytic applications of unsupported carbon nanofibers and nanotubes

Carbon materials are known to have an extremely high thermal conductivity, i.e. the in-plane thermal conductivity of graphite is about 3000 W m^{-1} K^{-1}. The similar structure of the carbon nanomaterials, when compared to that of graphite, suggests that their thermal conductivity should also be extremely high despite the lack of direct thermal conductivity measurements. Consequently, they can withstand a high heat transfer for use in highly exothermic reactions, i.e. Fischer–Tropsch or selective oxidation of H_2S into elemental sulfur. The small size and the high aspect ratio of the carbon nanotubes and nanofibers also significantly increases their external surface area which provides a high contact surface between the reactants and the deposited active sites. It is worth noting that carbon nanotubes also have one key advantage compared to the other materials, which is the presence of a straight hollow channel in their center with two open ends. The confinement effect which can be induced by the small size and high aspect ratio of the channel could give rise to unexpected modifications of liquids or gases passing through it which in turn can induce a tremendous improvement of the final catalytic activity or selectivity. Finally, the high chemical inertness of these materials renders possible their use in highly acidic or basic media without damage. These nanomaterials were predicted to be efficiently used in several potential application domains. Among them, the catalysis field seems to be the most promising according to the huge amount of research reported today in the open literature [4,5].

4. Why a need for macroscopic shaping of carbon nanofibers?

As mentioned above, the carbon nanofibers have been synthesized in a nanoscopic form, i.e. diameter <100 nm, thus, rendering hazardous their handling and large scale uses, especially in fixed-bed catalytic reactions. Apart from the danger of breathing them, their small size can induce detrimental pressure drops along the catalyst beds. Consequently, it was of interest to find methods allowing the synthesis of carbon nanostructures on a large scale along with a direct macroscopic shaping to immobilize them [31,32]. It was expected that this macroscopic shaping would open real opportunities for their use as promising catalyst support. Images of bulk carbon nanofibers in a powder form and of the different macroscopic supports are presented in Fig. 2. The macroscopic support should not alter the physical properties of the carbon nanostructures deposited on it, i.e. high mechanical strength in order to avoid breaking and catalytic bed plugging, high specific volume in order to afford a high space velocity of the gazeous reactants, high thermal conductivity which is the most important condition for catalyst operating in a highly exothermic or endothermic medium and finally, a high chemical resistance in order to be used in aggressive environments such as highly acidic or basic media. Different host carbon structures were used: cloth, felt, foam (see Fig. 2) but felt will be mainly described for the purpose of this presentation.

5. Synthesis of carbon nanofiber composite with macroscopic shaping

The macroscopic host structure used was a carbon felt (Carbone Lorraine Co.) which was constituted by a dense entangled network of micrometer carbon filaments with smooth surface (Fig. 3 A and B) which was used without any pretreatment. The starting carbon felt had almost no porosity which was in good agreement with the extremely low specific surface area observed, i.e. 1 m^2 g^{-1}. The carbon felt was cut into a predefinite shape, i.e. disk with a diameter of 1.5 cm and thickness of 0.12 cm, before depositing the nickel active phase. The nickel was deposited onto the carbon surface via an incipient wetness impregnation of a solution (ethanolic and water, 50:50) of nickel nitrate. The metal loading was set to be <1 wt.% of nickel metal. The metal loading was chosen to be high enough for the production of carbon nanofibers and low enough to avoid the need for further purification. In addition, the metal particles were completely encapsulated by the carbon nanofibers formed, and thus, were not accessible in the further catalytic uses of the composite. The solid was dried overnight at 100 °C. The macroscopic piece containing nickel was then loaded inside a tubular quartz reactor (100 mm inner diameter and 1200 mm length), placed in the center of an electric oven controlled by two thermocouples. The solid was calcinated in air at 300 °C for 2 h in order to decompose the nickel salt into its corresponding nickel

Fig. 2. Optical images of the unsupported carbon nanofibers in a powder form and the different macroscopic supports used in the composite synthesis.

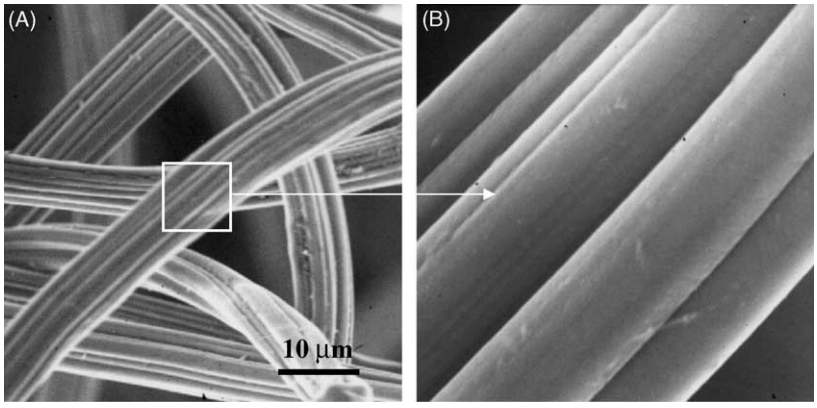

Fig. 3. SEM images of the microfilaments which constitute the starting macroscopic graphite felt. Note the extremely smooth surface of the filaments with almost no surface area and porosity.

oxide. The nickel oxide catalyst was then reduced in situ in flowing hydrogen (50 ml/min) at atmospheric pressure and 400 °C for 1 h. After reduction, the hydrogen flow was replaced by a mixture of C_2H_6:H_2 with different concentrations and total flow rate and the reactor temperature was increased from 400 °C to the desired synthesis temperature and held at this temperature for 2 h [33]. The material was then cooled from the synthesis temperature to room temperature under the reactant mixture. After cooling, the material was removed and stored in air. Helium (99.995%), hydrogen (99.995%) and ethane (99.998%) were purchased from Air Liquide. All the gases were used as received.

5.1. Carbon nanofibers yield

Supported nickel is well-known in the literature to be an active catalyst for carbon nanofiber formation through catalytic decomposition route [5,31]. In our previous work, nickel catalyst supported on carbon nanotubes was successfully used to synthesize large amounts, i.e. a 100 g of carbon nanofibers per gram of catalyst, by catalytic decomposition of hydrocarbons. The carbon-to-nickel growth ratio in the present work was about 50g/g of Ni/h which is in good agreement with our previous results. It is significant to note that the carbon nanofiber yield obtained in the present work was among the highest yield reported up to now in the literature taking into account the extremely low amount of the metal catalyst loading, i.e. 1 wt.%. The highest carbon nanofiber yield was obtained at a synthesis temperature of around 680 °C with a C_2H_6/H_2 (30/60 ml/ml) and a synthesis duration of 3 h. The presence of H_2 inside the reactant mixture was essential to obtain regular and thin carbon nanofibers. In the absence of H_2, the carbon nanofibers become less homogeneous with the appearance of irregular structures and nanoparticles. Similar results have also been reported by vander Wal and Hall [34] during the synthesis of carbon nanotubes on metal grid support using a mixture of C_6H_6 and C_2H_2 in the presence or not of hydrogen. The presence of H_2 also prevents the carbon build-up on the nickel surface which ultimately would lead to catalyst deactivation. However, the H_2 concentration should be low enough to avoid surface carbon removal by formation of CH_4 during the synthesis which would lead to a lower carbon nanofibers yield.

The high yield of carbon nanofibers observed was attributed to nickel particle breakup during the calcination process which exposed faceted structures by lattice dislocations, pits and crevice formation. Upon reduction in flowing H_2 at 400 °C, the lattice structure of the oxide underwent breakup along the oxide grain boundaries leading

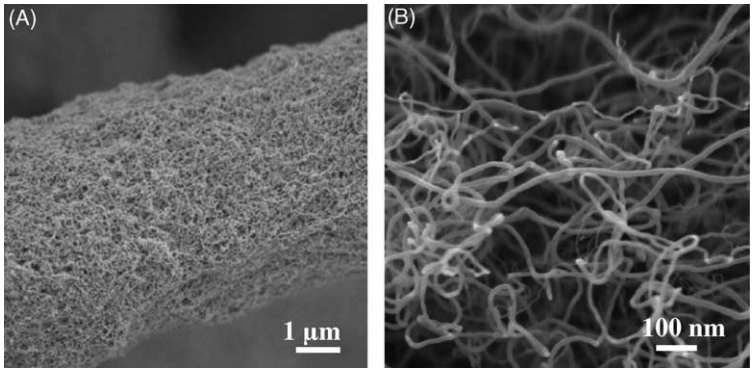

Fig. 4. (A) SEM image of the carbon nanofibers composite supported on a macroscopic graphite felt. (B) High resolution SEM image of the carbon nanofibers with an extremely homogeneous diameter centered at around 30 nm.

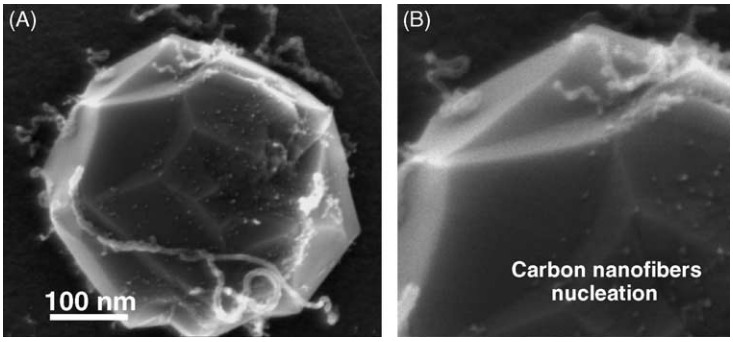

Fig. 5. SEM images of the carbon nanofibers growing in an octopus-like structure from a single nickel particle; and no relationship between the nickel particle size and the CNF diameter was observed. Note that all of the nickel faces were not able to grow nanofibers, in good agreement with the literature results which stated that only certain faces of the metal were active for carbon secretion whereas other faces were active for hydrocarbon decomposition.

to the formation of narrow active metal particles. The high density of defects of the final nickel particle probably played an important role in the final yield of the carbon nanofibers as it is thought that during the growth, the nickel particles became carburized by the reactant mixture and the carburization rate was expected to be higher in the presence of surface defects.

5.2. Carbon nanofibers composite characteristics

The SEM images of the as-prepared composite are presented in Fig. 4A and B with different magnifications. The low-magnification SEM image shows the complete filament morphology conservation as observed above (Fig. 4A). However, it should be noted that the diameter of the starting filament of the graphite felt was somewhat increased due to the formation of the CNFs on the outer surface. It is also significant to note that about 95% of the starting graphite filaments was covered by the CNFs. The high magnification SEM image gives access to the mean diameter of the formed CNFs material. These CNFs have very homogeneous diameters ranging around 30 nm and lengths up to several hundred nanometers which indicates the significant high aspect ratio of the material obtained (Fig. 4B). The synthesis was extremely selective towards carbon nanofiber formation as no carbon nanoparticles were observed on the sample after synthesis.

The complete coverage of the starting micrometer filaments by carbon nanofibers despite the low nickel loading was attributed to the exceptional length of the as-synthesised carbon nanofibers which rapidly covered the entire surface of the host filament according to the SEM image displayed in Fig. 5A where carbon nanofibers with a diameter of ca. 30 nm were grown in a web-like network from an aggregate of nickel with particle sizes of about 500 nm. The octopus growth of carbon nanofibers from a single crystal of Ni can also be visualized on the SEM micrograph taken after 10 min of synthesis presented in Fig. 5B where several carbon nanofiber growth centers can be observed. It was expected that during the synthesis, carbon nanofibers would be grown from several nickel islands dispersed in a discrete manner on the starting filaments microfibers, and due to their extremely high aspect ratio, would cover the initial within a short time.

A schematic representation of the proposed growth mechanism is shown in Fig. 6. Similar growth mode, i.e. octopus-like, have also been reported by different groups in the literature [35–37]. Ting and Liu [35] have suggested that during the synthesis, nickel is carburized into NiC, at least superficially, with a FCC structure which allows the subsequent growth of multiple carbon nanofibers from the [1 1 1] planes of the particle leading to the octopus-like carbon nanofiber structure. Nickel crystallographic faces reconstruction can be induced during the carbon nanofibers precipitation. The exact role of the different crystallographic metal or carbide surfaces on nanofibers growth needs to be clarified.

In order to get more insight about the growth mode of the carbon nanofibers from the nickel surface and the relationship between the diameter of the CNF and the diameter of the nickel particle, an experiment was conducted not on the supported nickel but directly on bulk metal with particle size

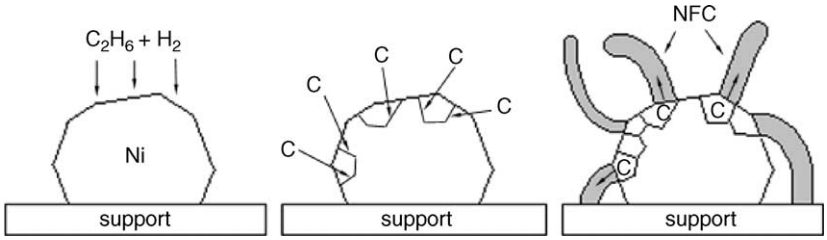

Fig. 6. Proposed growth mechanism of the CNF from a single nickel particle involving nickel fragmentation and reconstruction.

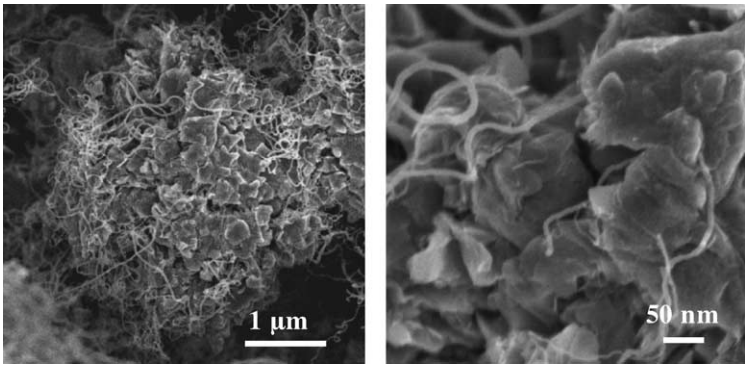

Fig. 7. SEM micrographs of the CNF growing from large bulk nickel particle. Note the complete independence between the nickel particle size and the diameter of the CNF.

of several micrometers. The SEM image of the sample (Fig. 7) clearly evidences the fact that the CNF diameter was not linked to the starting diameter of the nickel catalyst and confirms the above mechanism involving the fragmentation of the parent nickel particle into small particles which were responsible for the growth of CNF with homogeneous and small diameters. Statistical SEM images reported above have show that the carbon nanofiber diameter was relatively homogeneous and almost independence of the catalyst metal particle size.

The microstructure of the as-prepared CNFs was investigated by means of the TEM technique. TEM imaging provides more insight about the microstructure of the material: low magnification TEM image (Fig. 8A) shows that the CNFs were extremely pure and no trace of carbon nanoparticles was observed. High resolution TEM image (Fig. 8B) shows that the graphene planes were stacked at a certain angle with respect to the fiber axis with prismatic planes exposed at the surface. The interplanar distance between two adjacent graphene planes was about 0.335–0.34 nm in good agreement with the value

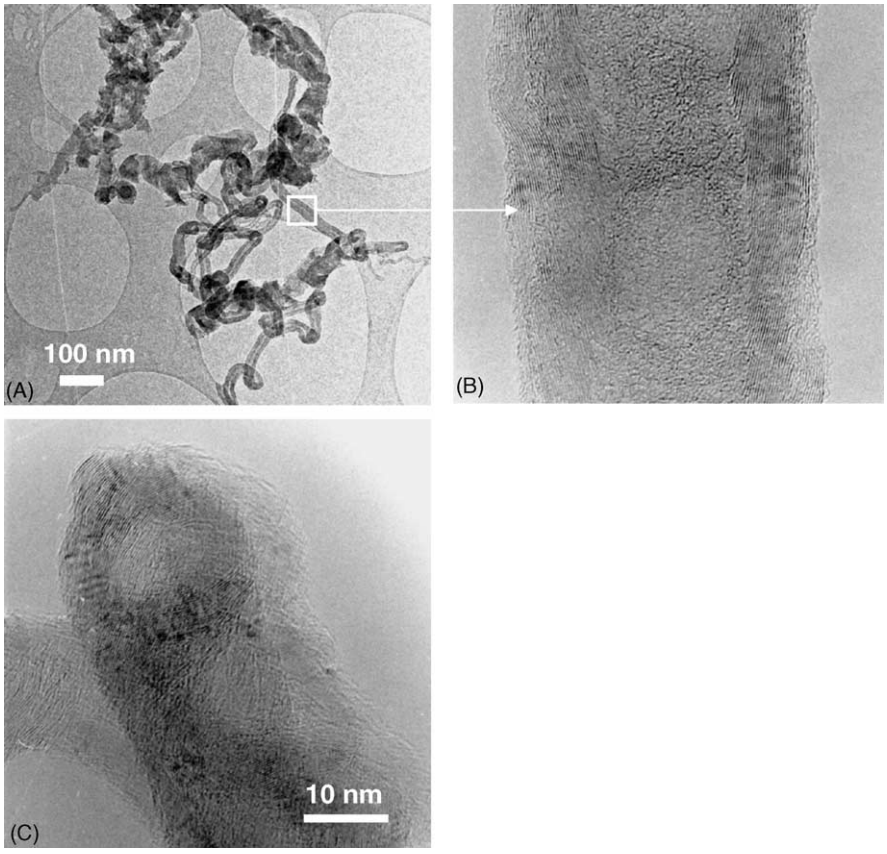

Fig. 8. TEM images of the carbon nanofibers with different magnifications. (A) Low magnification image showing the high selectivity of the as-synthesized carbon nanofibers. (B) High magnification TEM image showing the orientation of the graphene planes with respect to the fiber axis. (C) TEM image showing the lack of nickel particle on the fiber tip.

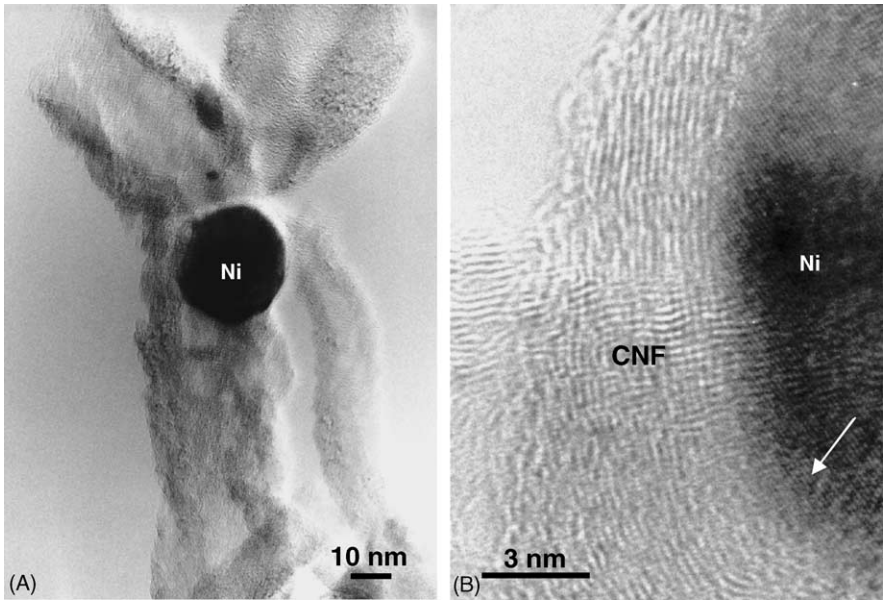

Fig. 9. TEM images showing the growth of several CNF from different faces of a single crystal of nickel (A). High magnification image showing the presence of defects inside the nickel matrix (lower part) attributed to the formation of a solid solution with the dissolved carbon atoms (B).

reported in the literature. It is significant to note that the prismatic planes of the fiber were well-exposed and only a very small amount of amorphous carbon covered the topmost surface of the fiber. Statistical TEM observation revealed the lack of nickel particles located at the carbon nanofiber tip (Fig. 8C) indicating that the tip growth mechanism did not occur. It was expected that the carbon source would be dissociated on certain faces of the nickel particles and carbon nanofibers emerge from other faces without nickel extraction in good agreement with the SEM results reported above on the sample after 10 min of reaction. It should be noted that almost no inner capping was observed inside the nanofiber tubule. vander Wal and Hall [34] reported that inner capping was observed when the supply rate of carbon was low. In the present case, the rate was probably high enough to avoid this inner capping.

The octopus growth can also be visualized by TEM and the results are displayed in Fig. 9. The low magnification TEM micrograph (Fig. 9A) shows the carbon nanofiber growth in several directions from a faceted nickel particle. The image clearly shows that the CNFs grow on distinct faces of the nickel particle while the hydrocarbon decomposition seems to occur on the top and bottom faces of the nickel particle. The high magnification TEM image shows the formation of defects in the nickel matrix next to the zone of carbon precipitation (Fig. 9B). These defects can be attributed to the supersaturation of the nickel matrix by the soluble carbon forming a solid solution with different metal interplanar distances compared to what is found in the pure parent metal.

The carbon nanofiber composite can be prepared with a well-controlled size and shape depending on the catalytic application. Fig. 10 represents some examples of the different carbon nanofiber composites which can be synthesized according to the method used.

6. Catalytic applications

The high external surface area of the carbon nanofibers, with prismatic planes exposed at the surface, renders them attractive for use as catalyst support. Several reports have

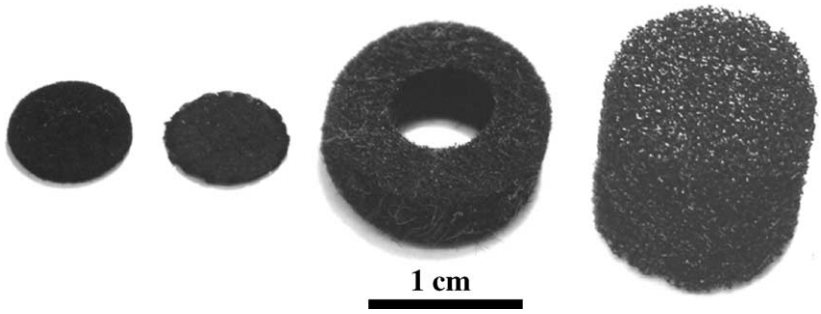

Fig. 10. Macroscopic size and shape of the different carbon nanofiber composite, i.e. disk (from felt or cloth), ring (from felt) and foam, synthesized according to the CVD method [31,32].

shown that carbon nanofibers when used as catalyst support display a high catalytic performance compared to the performance found on traditional catalysts supported on alumina, silica or activated charcoal [16–24]. The catalytic decomposition of hydrazine and the selective oxidation of H_2S into elemental sulfur in a discontinuous mode ($T \leq 60$ °C using Ni as an active phase) will be presented below to illustrate the advantage of using carbon nanofibers as catalyst support.

6.1. Hydrazine decomposition

The catalytic decomposition of hydrazine, N_2H_4, into N_2 and H_2 is the most studied reaction for satellite maneuvering and path correction [38–40]. The reaction is carried out by direct decomposition of liquid hydrazine over a highly loaded, i.e. 37 wt.%, stabilized alumina supported iridium catalyst which is produced industrially by Shell Co. The hydrazine decomposition pathway can be described as follows: first step decomposition into ammonia and nitrogen (1) and in the second step ammonia is decomposed into hydrogen and nitrogen (2) [41–43]. The first reaction, the hydrazine decomposition, is a structure insensitive reaction, i.e. is independent of particle size. The ammonia decomposition is a structure sensitive reaction depending on the average size or diameter of the dispersed active metal. Therefore, the characteristics of an hydrazine decomposition catalyst depend mainly on its activity in ammonia decomposition because the hydrazine decomposition reaction is easy.

$$3N_2H_4 \rightarrow 4NH_3 + N_2 \quad (1)$$

$$3N_2H_4 \rightarrow 3N_2 + 6H_2 \quad (2)$$

The extremely high exothermicity of the overall reaction leads to very hot gases and pressure release and provides the energy for the satellite propulsion. In addition, the reaction should take place in a millisecond range, and consequently, is mainly controlled by heat and mass diffusion processes: pressure on the catalyst bed and its temperature instantaneously increase with hydrazine introduction, from atmospheric pressure and room temperature to respectively several dozen of atmospheres and about 900 °C. The catalyst efficiency under these extreme conditions of use is limited by several critical drawbacks due to the alumina support, such as low thermal conductivity, limiting heat diffusion and leading to formation of hot spots on the catalyst surface, attrition problems resulting in the formation of fine powder, due to explosive reaction inside the pores of the support, and structural unstability at high temperature, transformation of phase from γ to α. It is, therefore, of interest to find a new catalyst support able to replace the alumina. The new support should display all the advantages of the former one, i.e. high surface area, good metal dispersion, without the drawbacks described above.

The decomposition of hydrazine was carried out in a 2 N thruster rocket (inner diameter of 6.7 mm, length of 20 mm) designed for the testing of supported iridium catalysts. The microthruster was located in a vacuum chamber kept under 0.1 mbar, attached to a thrust balance in order to reproduce as close as possible the real working conditions with the exception of microgravity (Fig. 11). The catalyst bed was preheated at 120 °C in the same way as that encountered during the real working conditions. The hydrazine injection pressure during the tests was kept at 22 or 5.5 bar, initial and final operating pressure in a real satellite. Hydrazine was injected onto the catalyst through an electrovalve in

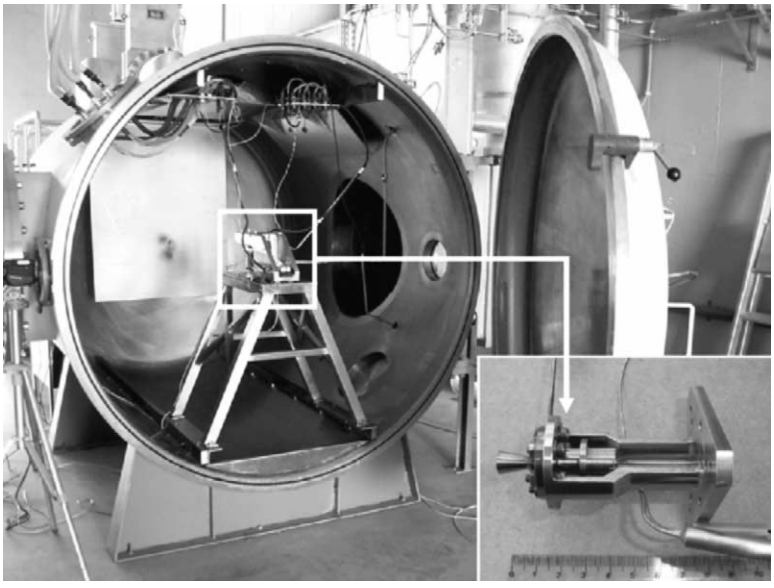

Fig. 11. Apparatus setup for the catalytic decomposition of hydrazine in a 2 N microthruster. The 2 N microthruster was located inside the vacuum chamber allowing the simulation of the space working conditions.

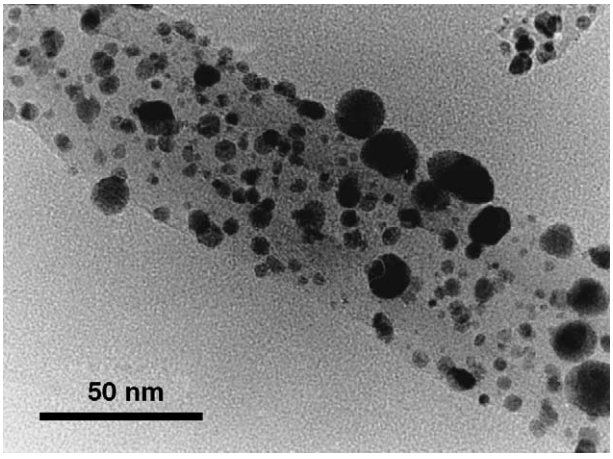

Fig. 12. TEM image of the iridium particles on the CNF composite after accelerated sintering under H_2 and steam at 500 °C for 24 h. The average iridium particle size was 7 nm.

successive pulses or continuously. Thrust, steady-state chamber pressure and temperature of the propulsion chamber were constantly recorded.

The iridium loaded catalyst (30 wt.% of metal) was prepared by incipient wetness impregnation of the carbon composite felt with an iridium salt H_2IrCl_6. After drying, oxidation in air at 350 °C for 2 h and final reduction/sintering in flowing hydrogen at 500 °C for 24 h, the catalyst still exhibited a medium metal dispersion (Fig. 12) with a particle size distribution ranging from 2 to 7 nm in diameter. Such a relatively high dispersion was attributed to the strong interaction between the iridium particles and the prismatic planes exposed by the carbon nanofibers and made of hydrophilic oxygenated surface groups [44]. These oxygenated groups also allowed an easy anchorage of the supported phases on the carbon support, as compared to what is observed with the less reactive basal planes of graphite or carbon nanotubes. Similar results have also been reported in the literature dealing with the metal dispersion on the carbon nanofiber surface.

6.1.1. Hydrazine decomposition test

For the bench-scale test, due to the difference in density between the two catalysts the weight of the commercial catalyst was 1.144 g (332 mg of Ir), whereas, the weight

Fig. 13. Schematic representation of the 2N microthruster used in the catalytic decomposition of hydrazine.

of the CNF-based catalyst was only 0.145 g (44 mg of Ir). The Ir/Al_2O_3 catalyst, in bead form, was packed inside the microtruster chamber using a shaking device in order to prevent the occurrence of empty spaces inside the catalyst bed. A schematic representation of the microthruster is presented in Fig. 13.

Attitude control applications of monopropellant hydrazine engines require operation over a wide range of duty cycles and pulse widths. Table 1 compares the multipulse average thrust of two tested catalysts for 100 runs for different monopropellant injection pressures and pulse-on/pulse-off electrovalve modes.

The results in Table 1 show better performances of the CNF-based catalyst. The thrust released during the hydrazine decomposition over the Ir/CNF composite was about three times higher than on the Ir/Al_2O3 catalyst, regardless of the difference between the iridium loading in the propulsion chamber due to the difference weight of the tested catalysts. The high performances, i.e. thrust (Table 1) and pressure (Fig. 14), of the Ir/CNF catalyst were attributed to the high accessibility of the catalytic sites towards the reactant due to the high external surface area of the support and the absence of any closed porosity inside the catalyst. On the alumina-based catalyst, due to the presence of a micro- and meso-porous network most of hydrazine did not reach the active sites, and thus, led to a lower pressure, as the unreacted hydrazine escaped from the catalyst bed without reacting. The high thermal conductivity of the carbon nanofibers support also allowed the rapid homogenization of the temperature through the entire catalyst bed, whereas, on the alumina-based catalyst, the temperature was not homogeneous due to the insulator character of the support, especially during the continuous tests, i.e. 5000 ms (Table 1).

The pressure response time is the time measured between the opening of the propellant electrovalve and the instant when 90% of the steady-state chamber pressure is obtained [20]. The time average from signal to 90% steady-state pressure was 46 ms for the Ir/CNF and 62 ms for the Shell

Table 1
Thrust (F) average values in N and propulsion chamber temperature (T_c) in °C of a 100 run series in different pressure levels and pulses widths were t_{on} is pulse-on time mode and t_{off} is pulse-off time mode in ms

	$P_{inj.}$ (bar)	t_{on} 20–t_{off} 980		t_{on} 200–t_{off} 800		t_{on} 500–t_{off} 500		t_{on} 5000	
		F	T_c	F	T_c	F	T_c	F	T_c
Shell 405	5.5	0.34	380	0.63	610	0.66	680	0.44	370
Ir/NFC	5.5	0.40	340	0.85	610	0.75	660	0.45	250
Shell 405	22	0.44	440	2.25	730	2.25	780	1.40	480
Ir/NFC	22	1.20	420	2.65	560	2.20	640	1.40	350

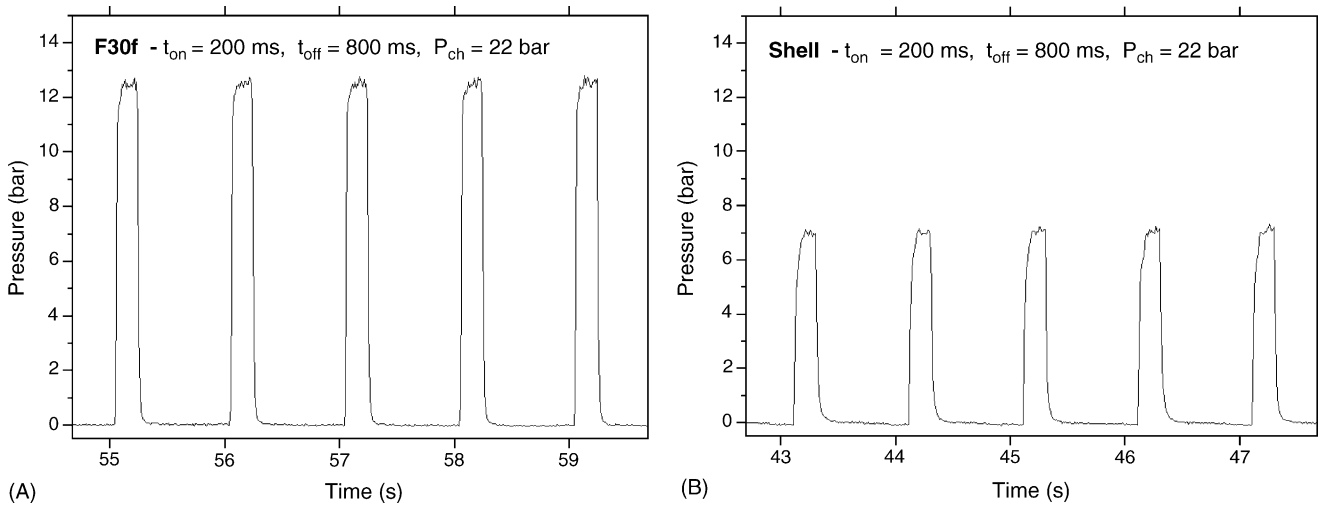

Fig. 14. Total pressure generated by the decomposition of the hydrazine in the vacuum chamber over the Ir/CNF composite and the Ir/Al_2O_3 catalysts.

catalyst at 5.5 bar, and 41 ms for the Ir/CNF and 43 ms for the Shell catalyst at 22 bar. The CNF-based catalyst overpasses the Shell 405 catalyst for its spontaneous restart capability. The time response of the Shell catalyst increases with the propellant injection pressure which allows the propellant to penetrate the pores network, and consequently, reaches more active sites.

The high catalytic performance of the CNF composite catalyst compared to that of the industrial catalyst was due to: (i) the high external surface area of the CNF composite catalyst and the complete absence of bottled pores providing a more effective contact between the reactant and the active sites without diffusional problems, (ii) the high thermal conductibility of the CNF composite catalyst allowing a rapid homogenization of the temperature release to the totality of the catalyst bed helping the final thermal decomposition of the rest of the reactants. The high thermal conductibility of the support also avoids temperature runaway on the catalyst surface which could induce drastic sintering of the active phase. The last point was confirmed on

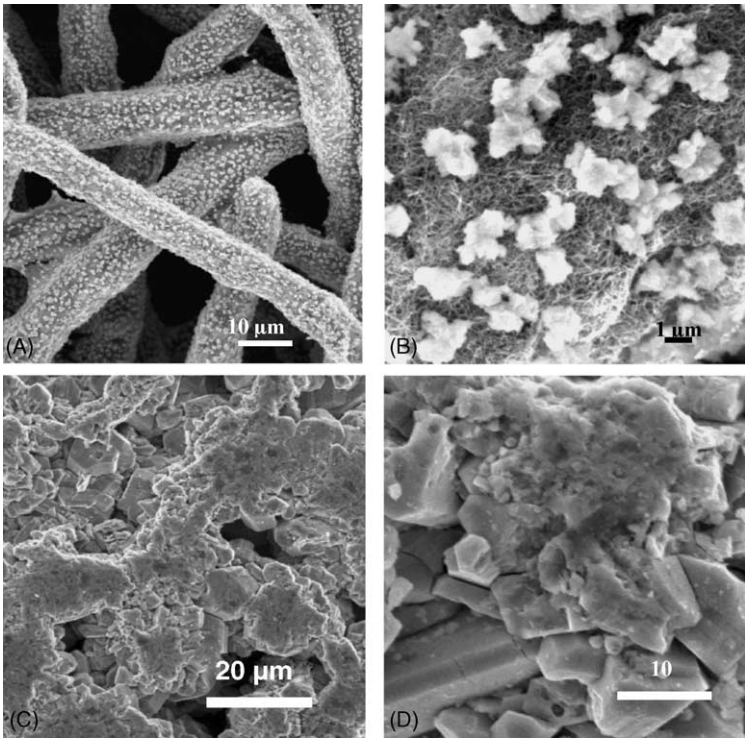

Fig. 15. (A and B) Ir/CNF and (C and D) Ir/Al_2O_3 catalysts after hydrazine firing (30 pulses) tests in the laboratory reactor setup. A severe sintering was occurred especially on the alumina-based catalyst where large aggregates of iridium were observed.

the same catalysts after reaction in the laboratory setup. On the CNF composite catalyst, an additional sintering was observed after hydrazine firing as evidenced by the SEM image in Fig. 15. However, the iridium particles remained well-dispersed with a homogeneous size of ca. 1 μm. On the other hand, the alumina-based catalyst exhibits a drastic sintering after test with the active phase forming large aggregates (Fig. 15B). The drastic sintering of the iridium phase on the alumina-based catalyst was attributed to the inability of the support to withstand the heat formed during the reaction, leading to the formation of hot spots.

6.2. Selective oxidation of H_2S into elemental sulfur

Hydrogen sulfide, H_2S, is generally released from natural gas plants and petroleum refineries. Due to its high toxicity, H_2S must be removed as far as possible before releasing the off gas into the atmosphere. The general trend is to selectively transform the H_2S into elemental sulfur by the equilibrated Claus process: $2H_2S + SO_2 \leftrightarrow (3/n)\ S_n + 2H_2O$ [45]. However, thermodynamic limitations of the Claus equilibrium reaction fix the maximum conversion level to about 97% which has led to the development of new processes to deal with the Claus tail-gas, based on the direct oxidation of the remaining traces ($\leq$1 vol.%) of H_2S in order to meet ever stricter legislation requirements. In the tail-gas processes, the remaining H_2S is catalytically oxidized into elemental sulfur in the presence of oxygen. Details concerning all these processes were summarized in a series of review articles but the catalysts, which are the core of the process, still need to be improved [46,47].

Recently, it has been reported that silicon carbide-based catalyst exhibits a high catalytic activity for this reaction either in a discontinuous-mode (reaction temperature $\leq$100 °C) or in a continuous-mode (reaction temperature $\geq$180 °C) [48–50]. In the discontinuous-mode, the silicon carbide catalyst allowed the transformation of the totality of H_2S (2500–3500 ppm) into elemental sulfur at reaction temperatures between 40 and 60 °C with a sulfur yield close to 100% [48,49]. In order to reduce the size of the reactor, the catalyst should be able to work under high space velocity. However, at space velocities higher than 0.005 h^{-1}, a significant drop in activity is rapidly observed which is attributed to a too low dispersion of the active phase and mainly to diffusion limitation inside the network of bottled pores of the SiC carrier.

To test the capacity of the catalyst supported on carbon nanofibers, the catalytic tests were carried out with a high space velocity, i.e. WHSV of 0.07 h^{-1} corresponding to a contact time of 1 s, at temperature of 60 °C. The reactant mixture composition was: H_2S (0.25 vol.%), O_2 (0.4 vol.%), H_2O (30 vol.%) and balance helium (Fig. 16). The NiS_2/β-SiC catalyst shows as expected a relatively high desulfurisation activity at the beginning of the test but deactivation rapidly occurred and the H_2S conversion became nil after about 50 h on stream. On the NiS_2/CNFs composite the H_2S conversion

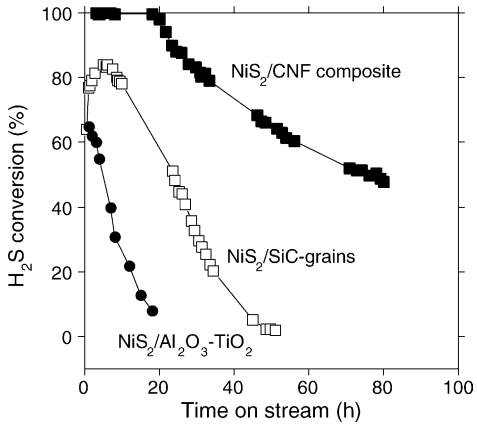

Fig. 16. Desulfurization activity (expressed in terms of H_2S conversion) on the NiS_2 supported on different supports. Reaction conditions: 60 °C, WHSV of 0.03 h^{-1} corresponding to the contact time of 1 s.

was total during the first 20 h on stream and then a slow deactivation was observed. However, the H_2S conversion still remained at about 50% even after 80 h of reaction while the total amount of solid sulfur deposited on the catalyst approached 150 wt.%. This high catalytic activity observed on the NiS_2/CNFs composite was attributed to the high external surface area of the support and the absence of bottled pores and confirmed the prediction. The slow deactivation slope was attributed to the progressive encapsulation of the active sites by the solid sulfur in good agreement with the literature results on these systems.

Previous results obtained on the NiS_2/β-SiC system have shown that the sulfur particles formed during the reaction were evacuated from the active site by the condensed water on the catalyst surface acting as a conveyor belt (Ref). The solid sulfur transported by the water film was subsequently deposited at the interface of the hydrophobic and hydrophilic area of the support. This transport phenomenon allowed to keep the catalytic activity stable despite the high amount of solid sulfur deposited on the catalyst surface.

The morphology of the deposited solid sulfur on the NiS_2/CNF composite catalyst after reaction was analyzed by SEM. Low magnification SEM image (Fig. 17A) shows that the sulfur was deposited in a discrete manner on the surface of the catalyst. According to the SEM image, a large part of the catalyst surface was covered by the sulfur aggregates which explains why a slow deactivation was observed on the carbon nanofiber-based catalyst after about 80 h of time on stream. However, it is worth noting that despite the relatively high solid sulfur deposit part of the catalyst surface was still accessible to the reactants. A high magnification SEM image shows that the sulfur particles adopted a peculiar anchorage on the catalyst surface. According to the SEM image the sulfur seems to be deposited originally not on the carbon nanofibers' surface but on the graphite microfilaments playing a role of the macroscopic support (the anchorage point is indicated by the arrow in Fig. 17B). This mode of sulfur anchorage can be explained as follows: the sulfur

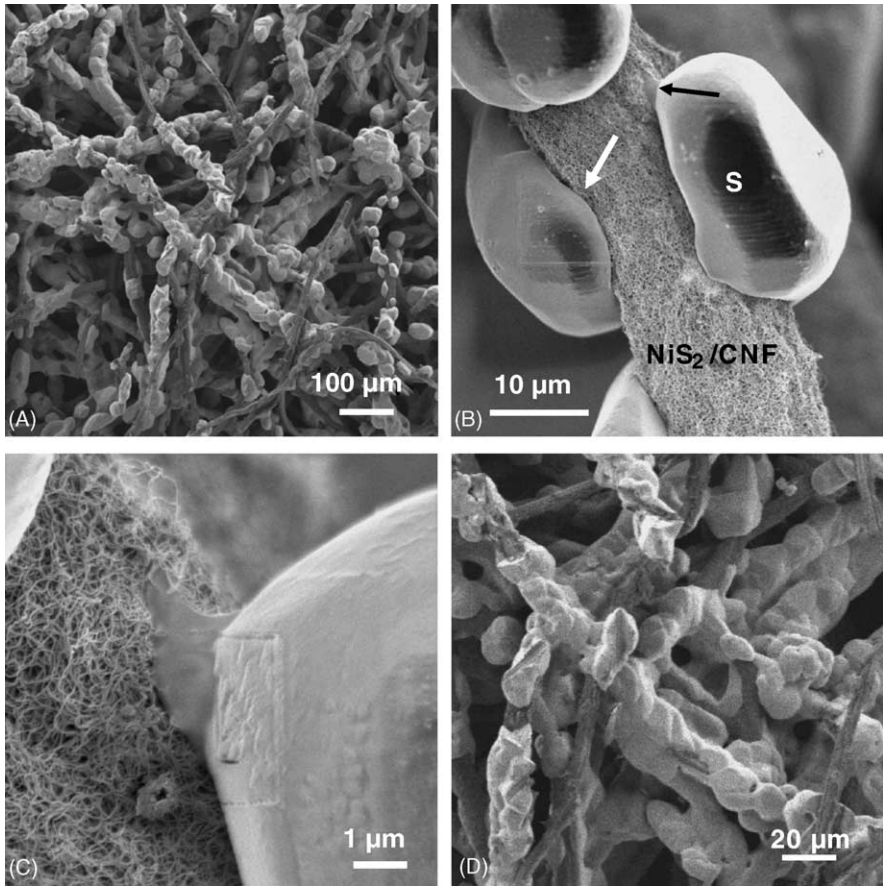

Fig. 17. SEM images of the solid sulfur morphology and location on the NiS_2/CNF composite catalyst after desulfurization at 60 °C. The amount of solid sulfur deposited was 150 wt.%. (A) Low magnification image showing the location of the solid sulfur on the catalyst surface. (B and C) High magnification images of the mode of anchorage of the solid sulfur on the catalyst. (D) Sulfur aggregates forming at high sulfur loading which was responsible for the deactivation observed.

formed on the NiS_2 site was rapidly washed by the condensed water film from the hydrophilic surface of the carbon nanofibers, i.e. prismatic planes with high affinity for water, and subsequently deposited on the underlying graphite microfilament with hydrophobic character. As a function of time on stream the solid sulfur grows away from the microfilament surface and remains on the outer surface of the support in the form of large round-shaped particles. The unwettability between the deposited solid sulfur and the CNF surface was highlighted by the absence of interface between these two elements as shown in Fig. 17B (white arrow). This peculiar form of deposited sulfur was attributed to the formation of solid sulfur in the presence of liquid water at low temperature. These sulfur particles continue to grow and finally completely encapsulate the catalyst surface as show in Fig. 17D, and as a consequence, led to the slow deactivation. The deactivated catalyst can be totally regenerated by heat treatment in flowing helium at 250 °C for 2 h. XRD pattern recorded on the regenerated sample clearly indicate the complete removal of the deposited solid sulfur and only NiS_2 phase was remained. The desulfurisation activity of the regenerated catalyst was identical to that observed on the fresh catalyst indicating the total conservation of the active phase nature and accessibility.

7. Conclusion

In summary, carbon nanofiber composites with macroscopic shaping can be efficiently employed as a new class of catalyst support which exhibits a high catalytic activity along with a peculiar product selectivity when compared to those observed on traditional catalysts. The high catalytic performances of the CNF-based catalyst were attributed to: (i) the high external surface area of the support which allows rapid access of the reactants to the active sites, (ii) the high thermal conductibility of the support which allows the rapid evacuation of the heat formed during the reaction and favours the temperature homogenisation throughout the catalyst bed and (iii) the high flexibility of the support which allows the catalyst to resist pressure shocks, i.e. decomposition of hydrazine. Finally, it should be noted that the complete absence of bottled pores allows the rapid 3D access of the entire volume of the catalyst to the reactants

and also for the rapid evacuation of the products which significantly lowers secondary reactions.

Acknowledgements

The work presented here could not have been realized without wide collaboration both inside the laboratory and outside the laboratory. The authors would like to thank Dr. R. Vieira, Dr. J.M. Nhut, M.P. Nguyen, M.P. Bernhardt, M.M. Wolf, all from the Laboratoire des Matériaux, Surfaces et Procédés pour la Catalyse (LMSPC-ELCASS) for their great help during the different experimental processes. The authors would like also to thank Mrs. G. Ehret, Dr. C. Estournès, Prof. J. Guille from the Institut de Physique et Chimie des Matériaux de Strasbourg for TEM and SEM experiments and also for helpful discussion during this work. Finally, CnpQ (Brazil), Lurgi GmbH (Germany), Ademe (France), Sicat SA (France) are gratefully acknowledged for the financial support of the different research presented here.

References

[1] M.J. Ledoux, C. Pham-Huu, CaTTech 5 (2001) 226.
[2] C. Pham-Huu, N. Keller, M.J. Ledoux, Acta Chim. 10 (2002) 8.
[3] S. Iijima, Nature 354 (1991) 36.
[4] P.M. Ajayan, Chem. Rev. 99 (1999) 1797.
[5] J.P. de Jong, J.W. Geus, Catal. Rev. Sci. Eng. 42 (2000) 481.
[6] H.J. Dai, Acc. Chem. Res. 35 (2002) 1045.
[7] C. Pham-Huu, N. Keller, V.V. Roddatis, G. Mestl, R. Schlögl, M.J. Ledoux, Phys. Chem., Chem. Phys. 4 (2002) 514.
[8] F. Salman, C. Park, R.T.K. Baker, Catal. Today 53 (1999) 385.
[9] C. Park, R. Terry, R.T.K. Baker, J. Phys. Chem. B 103 (1999) 2453.
[10] C. Pham-Huu, N. Keller, L. Charbonniére, R. Ziessel, M.J. Ledoux, Chem. Commun. (2000) 1871.
[11] Z.J. Liu, Z.Y. Yuan, W. Zhou, L.M. Peng, Z. Xu, Phys. Chem. 3 (2001) 2518.
[12] C.A. Bessel, K. Laubernds, N.M. Rodriguez, R.T.K. Baker, J. Phys. Chem. B 105 (2001) 1115.
[13] E. van Steen, F.F. Prinsloo, Catal. Today 71 (2002) 327.
[14] R. Vieira, C. Pham-Huu, N. Keller, M.J. Ledoux, Chem. Commun. (2002) 954.
[15] R. Giordano, P. Serp, P. Kalck, Y. Kihn, J. Schreiber, C. Marhic, J.L. Duvail, J. Eur, Inorg. Chem. (2003) 610.
[16] M.J. Ledoux, R. Vieira, C. Pham-Huu, N. Keller, J. Catal. 216 (2003) 333.
[17] C. Pham-Huu, N. Keller, R. Charbonnière, R. Ziessel, M.J. Ledoux, Chem. Commun. (2000) 1871.
[18] C. Pham-Huu, J. Mol. Catal. A Chem. 170 (2001) 155.
[19] R.T.K. Baker, M.A. Barber, P.S. Harris, F.S. Feates, R.J. Waite, J. Catal. 26 (1972) 51.
[20] N.M. Rodriguez, M.S. Kim, R.T.K. Baker, J. Phys. Chem. 98 (1994) 108.
[21] N.M. Rodriguez, A. Chambers, R.T.K. Baker, Langmuir 11 (1995) 3862.
[22] N. Krishnankutty, C. Park, N.M. Rodriguez, R.T.K. Baker, Catal. Today 37 (1997) 295.
[23] A. Chambers, T. Nemes, N.M. Rodriguez, R.T.K. Baker, J. Phys. Chem. B 102 (1998) 2251.
[24] C. Park, R. Terry, R.T.K. Baker, J. Phys. Chem. B 103 (1999) 2453.
[25] Q.H. Wang, A.A. Setlur, J.M. Lauerhaas, J.Y. Dai, E.W. Seelig, R.P.H. Chang, Appl. Phys. Lett. 72 (1998) 2912.
[26] J.M. Bonard, H. Kind, T. Stöckli, L.O. Nilsson, Solid State Electron. 45 (2001) 893.
[27] X. Gong, J. Liu, S. Baskaran, R.D. Voise, J.S. Young, Chem. Mater. 12 (2000) 1049.
[28] J. Bai, Carbon 41 (2003) 1325.
[29] M.J. Ledoux, R. Vieira, C. Pham-Huu, N. Keller, J. Catal. 216 (2003) 333.
[30] C. Park, M.A. Keane, J. Catal. 221 (2004) 386.
[31] R. Vieira, M.J. Ledoux, C. Pham-Huu, Appl. Catal. A 274 (2004) 1.
[32] C. Pham-Huu, R. Vieira, L. Charbonnière, R. Ziessel, M.J. Ledoux, French Patent Appl. No. 01-15178 (2001) assigned to Sicat SA.
[33] R. Vieira, Thesis, University of Strasbourg, 2003.
[34] R.L. vander Wal, L.J. Hall, Chem. Phys. Lett. 349 (2001) 178.
[35] J.M. Ting, R.M. Liu, Carbon 41 (2003) 601.
[36] D. Ding, J. Wang, Z. Cao, J. Dai, Carbon 41 (2003) 579.
[37] C. Emmenegger, J.M. Bonard, P. Mauron, P. Sudan, A. Lepora, B. Grobety, A. Züttel, L. Schlapbach, Carbon 41 (2003) 539.
[38] H.D. Schmidt, Hydrazine and Its Derivatives: Preparation Properties and Applications, Wiley, New York, 1984.
[39] T.G. Soares Neto, A.J.G. Cobo, G.M. Cruz, Appl. Catal. A 250 (2003) 331.
[40] L.F. Audrieth, B.A. Ogg, The Chemistry of Hydrazine, John Wiley & Sons, New York, 1951.
[41] S. Balcon, Thesis, University of Poitiers, 1999.
[42] C. Kappenstein, S. Balcon, S. Rossignol, E. Gengembre, Appl. Catal. A 182 (1999) 317.
[43] S. Balcon, S. Mary, C. Kappenstein, E. Gengembre, Appl. Catal. A 196 (2000) 179.
[44] R. Vieira, D.B. Netto, M.J. Ledoux, C. Pham-Huu, Appl. Catal. A 279 (2005) 35.
[45] Chasing the elusive last 1 or 2%, Sulphur 252 (1997).
[46] J. Wieckowska, Catal. Today 24 (1995) 405.
[47] A. Piéplu, O. Saur, J.C. Lavalley, O. Legendre, C. Nedez, Catal. Rev. Sci. Eng. 43 (4) (1998) 409.
[48] N. Keller, C. Pham-Huu, C. Crouzet, M.J. Ledoux, S. Savin-Poncet, J.B. Nougayrède, J. Bousquet, Catal. Today 53 (1999) 535.
[49] M.J. Ledoux, C. Pham-Huu, N. Keller, J.B. Nougayrède, S. Savin-Poncet, J. Bousquet, Catal. Today 61 (2000) 257.
[50] N. Keller, C. Pham-Huu, M.J. Ledoux, Appl. Catal. A 217 (2001) 205.